

**First-principles investigation of cubic BaRuO<sub>3</sub>: A Hund's metal**Nagamalleswararao Dasari,<sup>1,\*</sup> S. R. K. C. Sharma Yamijala,<sup>2</sup> Manish Jain,<sup>3</sup> T. Saha Dasgupta,<sup>4</sup> Juana Moreno,<sup>5,6</sup> Mark Jarrell,<sup>5,6</sup> and N. S. Vidhyadhiraja<sup>1,†</sup><sup>1</sup>Theoretical Sciences Unit, Jawaharlal Nehru Centre For Advanced Scientific Research, Jakkur, Bangalore 560064, India<sup>2</sup>Chemistry and Physics of Materials Unit, Jawaharlal Nehru Centre For Advanced Scientific Research, Jakkur, Bangalore 560064, India<sup>3</sup>Department of Physics, Indian Institute of Science, Bangalore 560012, India<sup>4</sup>S. N. Bose Centre for Basic Sciences, Kolkata 700 098, India<sup>5</sup>Department of Physics & Astronomy, Louisiana State University, Baton Rouge, Louisiana 70803-4001, USA<sup>6</sup>Center for Computation and Technology, Louisiana State University, Baton Rouge, Louisiana 70803, USA

(Received 15 December 2015; revised manuscript received 18 July 2016; published 24 August 2016)

A first-principles investigation of cubic BaRuO<sub>3</sub>, by combining density functional theory with dynamical mean-field theory and a hybridization expansion continuous time quantum Monte Carlo solver, has been carried out. Nonmagnetic calculations with appropriately chosen on-site Coulomb repulsion  $U$  and Hund's exchange  $J$  for single-particle dynamics and static susceptibility show that cubic BaRuO<sub>3</sub> is in a spin-frozen state at temperatures above the ferromagnetic transition point. A strong redshift with increasing  $J$  of the peak in the real frequency dynamical susceptibility indicates a dramatic suppression of the Fermi liquid coherence scale as compared to the bare parameters in cubic BaRuO<sub>3</sub>. The self-energy also shows clear deviation from Fermi liquid behavior that manifests in the single-particle spectrum. Such a clean separation of energy scales in this system provides scope for an incoherent spin-frozen (SF) phase that extends over a wide temperature range, to manifest in non-Fermi liquid behavior and to be the precursor for the magnetically ordered ground state.

DOI: [10.1103/PhysRevB.94.085143](https://doi.org/10.1103/PhysRevB.94.085143)**I. INTRODUCTION**

Transition metal oxides (TMOs) have occupied a unique and very significant position in the investigations of correlated electron systems. The interplay of spin, charge, and orbital degrees of freedom in the partially filled and localized  $3d$  and  $4d$  orbitals leads to a rich set of phenomena including high temperature superconductivity, colossal magnetoresistance, and the Mott metal-insulator transition. Due to the extended nature of  $4d$  orbitals, the corresponding TMOs exhibit strong hybridization with oxygen. This leads to a large crystal field splitting that could be of the order of the local screened Coulomb interaction ( $U$ ) and a broad  $4d$  band of width  $W$ . As a consequence, these materials prefer a low spin state rather than the high spin state.

Furthermore, the wide  $d$  band in  $4d$ -orbital based TMOs, such as the ruthenates, leads to a moderate screened Coulomb interaction  $U \simeq W$  as compared to the much narrower  $d$  band in  $3d$ -orbital based TMOs [1]. Surprisingly however, most of the Ru-based TMOs show strong correlation effects that are reflected in the enhanced linear coefficient of their specific heat  $\gamma$ . A few of such ruthenates are mentioned in Table I, where we have also indicated the magnetic order of the ground state as well as the effective mass computed as the ratio of experimentally [1,2] measured  $\gamma$  to  $\gamma_{\text{LDA}}$ , which is computed [2] within a local density approximation (LDA). The origin of such enhanced effective mass could be a local Coulomb repulsion induced proximity to an insulating state. An alternative origin could be the Hund's [1,3–5] coupling  $J$  (intra-atomic exchange), which, as has been shown recently for several materials, especially ruthenates [3,6,7], leads to their

characterization as ‘‘Hund's metals.’’ A prominent member of this class is BaRuO<sub>3</sub> which, depending on synthesis conditions, can exist in four polytypes [8]. These are nine-layered rhombohedral (9R), four-layered hexagonal (4H), six-layered hexagonal (6H), and cubic (3C). The 9R has a paramagnetic insulating (PI) ground state while 4H and 6H are paramagnetic metals (PM).

The 3C-BaRuO<sub>3</sub> polytype is a ferromagnetic metal with Curie temperature  $T_c = 60$  K, which is much smaller than the value of  $T_c (= 160$  K) in SrRuO<sub>3</sub> [9]. The experimental value of the saturated magnetic moment of 3C-BaRuO<sub>3</sub> [8] is  $0.8 \mu_B/\text{Ru}$ , which is far less than the  $2.8 \mu_B/\text{Ru}$  expected for a low spin state. It is also smaller than the measured value of  $1.4 \mu_B/\text{Ru}$  in SrRuO<sub>3</sub> [9]. The observed effective magnetic moment ( $\mu_{\text{eff}}$ ) in the paramagnetic phase of BaRuO<sub>3</sub> and SrRuO<sub>3</sub> is, however, very close to the moment of a  $S = 1$  state with a rotationally invariant  $J$  term. From Table I we can readily understand that electron correlations in 4H-BaRuO<sub>3</sub> and 6H-BaRuO<sub>3</sub> are comparable to the correlation in SrRuO<sub>3</sub>, and in case of 9R-BaRuO<sub>3</sub> they are weaker. Although the strength of the electron correlations in 3C-BaRuO<sub>3</sub> is still unknown, a non-Fermi liquid behavior in the experimentally measured resistivity [8,10], i.e.,  $\rho(T) \propto T^{1.85}$  in the ferromagnetic phase and its crossover to  $T^{0.5}$  in the paramagnetic phase (similar to SrRuO<sub>3</sub> [11] and CaRuO<sub>3</sub> [12] compounds), hints towards a strongly correlated system [1].

In the present work we address the following questions: Is 3C-BaRuO<sub>3</sub> a correlated metal or not? If yes, then what is the origin and strength of correlations? What is the probable origin of the non-Fermi liquid (NFL) signature in the resistivity [8,10]? We have employed the dynamical mean-field theory (DMFT) framework in combination with an *ab initio* method [13], namely density functional theory (DFT) within the generalized gradient approximation (GGA) [14]. In the DMFT [15] framework, a lattice problem is mapped on to a single

\*nagamalleswararao.d@gmail.com

†raja@jncasr.ac.in

TABLE I. Magnetic ground state and the ratio of  $\gamma$  to  $\gamma_{\text{LDA}}$  for  $4d$  Ru-based compounds. (PM: paramagnetic metal, FM: ferro-magnetic metal, and PI: paramagnetic insulator.)

Compound	Magnetic order	$\frac{\gamma}{\gamma_{\text{LDA}}}$
$\text{Sr}_2\text{RuO}_4$	PM	4
$\text{Sr}_3\text{Ru}_2\text{O}_7$	PM	10
$\text{CaRuO}_3$	PM	7
$\text{SrRuO}_3$	FM < 160 K	4
3C-BaRuO <sub>3</sub>	FM < 60 K	–
4H-BaRuO <sub>3</sub>	PM	3.37
6H-BaRuO <sub>3</sub>	PM	3.37
9R-BaRuO <sub>3</sub>	PI	1.54

impurity Anderson model with a self-consistently determined bath. We solve the resulting quantum impurity problem by using the hybridization expansion [16,17] continuous-time quantum Monte Carlo algorithm (HY-CTQMC). Our main finding is that 3C-BaRuO<sub>3</sub> is a Hund's correlated metal. Furthermore, we find that 3C-BaRuO<sub>3</sub> is in a spin-frozen state at temperatures in the neighbourhood of the ferromagnetic transition temperature. This state, we speculate, is the precursor of the ferromagnetic ground state and also a possible origin of the experimentally observed NFL behavior in resistivity.

The rest of the paper is organized as follows. In Sec. II we describe the DFT details and Wannier projection briefly. In Sec. III we describe our results from GGA+DMFT(CTQMC) for 3C-BaRuO<sub>3</sub>. We present our conclusions in the final section.

## II. DETAILS OF THE DENSITY FUNCTIONAL THEORY CALCULATIONS AND RESULTS

The 3C polytype of BaRuO<sub>3</sub> belongs to the space group of  $Pm\bar{3}m$  which corresponds to an ideal cubic perovskite structure, while the closely related CaRuO<sub>3</sub> and SrRuO<sub>3</sub> crystallize in an orthorhombic distorted perovskite structure of space group  $Pnma$  [8]. A significant structural change from CaRuO<sub>3</sub> to SrRuO<sub>3</sub> and to BaRuO<sub>3</sub> is a decrease in the bending angle [8] ( $180^\circ - \phi$ ) of Ru-O-Ru bonds, which becomes zero for BaRuO<sub>3</sub>. Apart from the slight distortions of the RuO<sub>6</sub> octahedra in CaRuO<sub>3</sub> and SrRuO<sub>3</sub>, which are absent in BaRuO<sub>3</sub> [8], each of these materials have threefold degenerate  $t_{2g}$  bands near the Fermi level with a formal valence of four electrons [8], i.e.,  $t_{2g}^4 e_g^0$ . We perform density functional theory (DFT) calculations within the generalized gradient approximation using the plane-wave pseudopotential code QUANTUM ESPRESSO [18]. We use ultrasoft pseudopotentials with the Perdew-Burke-Ernzerhof [19] exchange-correlation functional. An  $8 \times 8 \times 8$  Monkhorst-Pack  $k$  grid is used for optimization together with an 80 Ry energy cutoff and a 640 Ry charge cutoff. The system is considered to be optimized if the forces acting on all the atoms are less than  $10^{-4}$  Ry/bohr. After optimization we find the lattice parameter to be 4.0745 Å. Throughout the calculations, the Marzari-Vanderbilt cold smearing is used with a degauss value of 0.01 Ry. A  $20 \times 20 \times 20$   $k$  grid without any symmetries is used for all the non-self-consistent calculations (including Wannier90 calculations). To extract the information of the low-energy subspace,

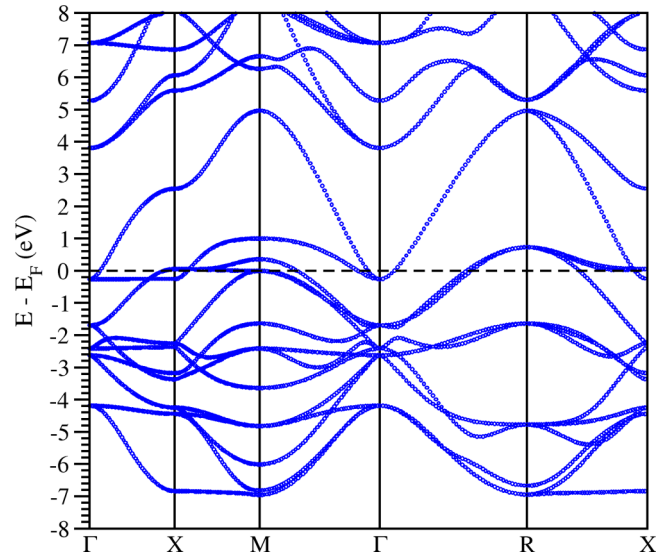


FIG. 1. Band structure of cubic BaRuO<sub>3</sub> in its nonmagnetic phase. Energies are scaled to the Fermi level (dotted line).

which is used in the DMFT calculation, we have projected the Bloch wave functions obtained from our DFT calculations onto the Ru- $t_{2g}$  orbitals using the maximally localized Wannier functions (MLWF) [20] technique as implemented in the Wannier90 code [21].

The electronic band structure, density of states (DOS), and projected DOS (pDOS) of BaRuO<sub>3</sub> in its nonmagnetic (NM) phase are given in Figs. 1 and 2. The DFT results predict BaRuO<sub>3</sub> to be a metal in its nonmagnetic phase with major contributions from the Ru-4d and O-2p orbitals across the Fermi level. Hybridization between Ru-4d orbitals and O-2p orbitals spans from approximately 8 eV below the Fermi level

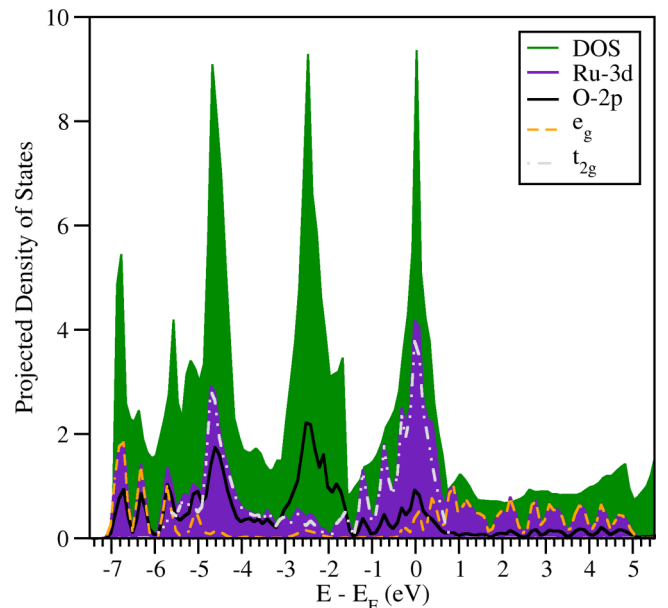


FIG. 2. Projected density of states (PDOS) of BaRuO<sub>3</sub>. Green (shaded light gray), violet (shaded dark gray), black (thick line), orange (dashed line), and gray (dot-dashed line) represent the DOS of the whole system, Ru-atom, O-atom, Ru- $e_g$ , and Ru- $t_{2g}$ , respectively.

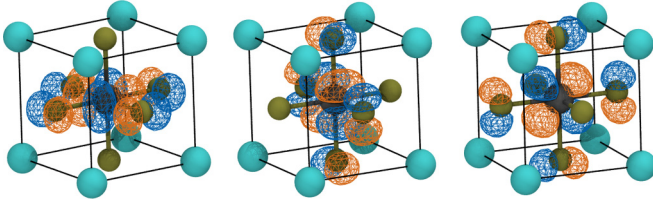


FIG. 3. Orbital plots of maximally localized Wannier functions used to reproduce the low-energy subspace Hamiltonian.

to around 5 eV above the Fermi level. Bands above 5 eV are mainly composed of Ba- $d$  and Ru- $p$  orbitals.

We find that, due to the octahedral environment of the oxygen ions surrounding the ruthenium, the Ru- $4d$  orbitals split into two sets, namely  $t_{2g}$  and  $e_g$ , where  $t_{2g}$  ( $e_g$ ) orbital's contribution to the DOS is mainly below (above) the Fermi level, supporting the low-spin  $t_{2g}$  configuration of the nominal valence Ru $^{4+}$  ( $d^4$ ).

From Fig. 2 we infer that the low-energy subspace ( $-2.5$  to  $1$  eV), which is relevant for the DMFT calculations, is mainly composed of Ru- $t_{2g}$  orbitals (with minor contributions from O- $2p$  and Ru- $e_g$  orbitals) with occupancy of approximately four electrons. Hence, to extract the low-energy subspace Hamiltonian in an effective Wannier function basis, we project the Bloch wave functions obtained from our DFT calculations onto the  $d_{xz}$ ,  $d_{yz}$ , and  $d_{xy}$  orbitals. The optimized Wannier functions calculated using the MLWF method as implemented in the Wannier90 [21] code are given in Fig. 3 and the corresponding low-energy subspace band structure calculated using these Wannier functions are given in Fig. 4. Clearly the band structures obtained from both the basis sets (Wannier, plane wave) compare fairly well in the low-energy subspace, validating the proper choice of our projection. Also, as shown in Fig. 3, the Wannier functions show the  $d_{xz}$ ,  $d_{yz}$ , and  $d_{xy}$  orbital character and in addition have a substantial O- $2p$  character due to their contributions near the Fermi level. The Hamiltonian obtained in this Wannier basis is used for all the DMFT calculations, as the unperturbed or the “noninteracting” Hamiltonian.

### III. GGA+DMFT

In the DMFT calculations we introduced a local Coulomb interaction of density-density type between the orbitals. The interaction part of the Hamiltonian is given in the second

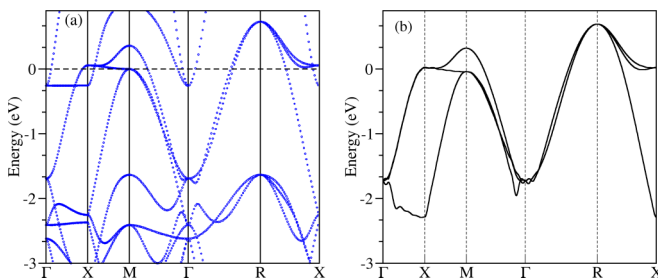


FIG. 4. Low-energy subspace band structure obtained from: (a) Plane-wave basis and (b) Wannier basis.

quantization notation by

$$H_{ii}^{\text{int}} = \sum_{i,\alpha=1}^3 U n_{i\alpha\uparrow} n_{i\alpha\downarrow} + \sum_{i,\alpha\neq\beta} \sum_{\sigma\sigma'} (V - J\delta_{\sigma\sigma'}) n_{i\alpha\sigma} n_{i\beta\sigma'},$$

where  $i$  represents the lattice site and  $\alpha, \beta$  represent orbital indices.  $U$  is the Coulomb repulsion between two electrons with opposite spin on the same orbital. We impose orbital rotational symmetry by setting  $V = U - 2J$ , where  $J$  is the Hund's coupling, which lowers the energy of a configuration with different orbitals ( $\alpha \neq \beta$ ), and parallel spins  $\sigma = \sigma'$ . We solve the effective impurity problem within DMFT by using the hybridization expansion continuous-time quantum Monte Carlo (HY-CTQMC). In the literature, a range of  $U$  and  $J$  values have been used for  $4d$ -Ru based TMOs. Indeed, determining these without ambiguity is not possible at present. In a recent work [7], using the constrained random phase approximation (cRPA) method, the  $U$  value for ruthenates was found to be 2.3 eV. Thus, we choose  $U_{\text{Ru}} = 2.3$  eV. We fix the  $J_{\text{Ru}} \sim 0.5$  to a value such that the theoretically calculated paramagnetic magnetic moment matches the corresponding experimentally measured value. Apart from this specific set of model parameters, we have investigated a range of  $(U, J)$  values in the neighborhood of  $(U_{\text{Ru}}, J_{\text{Ru}})$  to ascertain the position of 3C-BaRuO $_3$  in the phase diagram. In the DMFT calculations, we find the chemical potential by fixing the occupancy to four electrons per Ru. Before we discuss our results on cubic BaRuO $_3$  with density-density type interactions, we briefly review investigations on the role of rotationally invariant interactions for multiband models within DMFT. Werner *et al.* [3] have studied a three-band model with a full rotationally invariant Hamiltonian for a toy density of states. They found a quantum phase transition between a paramagnetic metallic phase and a spin-frozen phase with a rotationally invariant on-site exchange  $0 < J < \frac{U}{3}$ . The characteristic features of the spin-frozen phase are that the single-particle self-energy has non-Fermi liquid (power-law) behavior and the local spin-spin correlation function  $\langle S_i^z(0)S_i^z(\tau) \rangle$  does not decay at long times. Later, the same model was studied by Mravlje *et al.* [6] in a ruthenium-based compound and interestingly they found a generalized Fermi liquid as the ground state of the system for any finite  $J$ . Antipov *et al.* [22] have shown that spin-flip terms are essential in restoring the Fermi liquid behavior at zero temperature [23,24]. They also found that spin-flip and pair-hopping terms lead to enhancement of effective mass and a decrease of magnetic ordering temperature in comparison with density-density type interactions. So, a quantitative estimation of  $m^*$  is not possible with density-density type interactions.

Now we are going to discuss our results for single and two-particle dynamical quantities obtained from GGA+DMFT by using HY-CTQMC as an impurity solver.

#### A. Single-particle dynamics

To begin with, we focus on the single-particle dynamics that is mainly determined by the self-energy  $\Sigma(i\omega_n)$ . Figure 5(a) shows the imaginary part of Matsubara self-energy for  $U = 2.3$  eV and  $T = 60$  K for a range of  $J$  values. For  $J \lesssim 0.1$ , the low-frequency behavior of the self-energy has a generalized

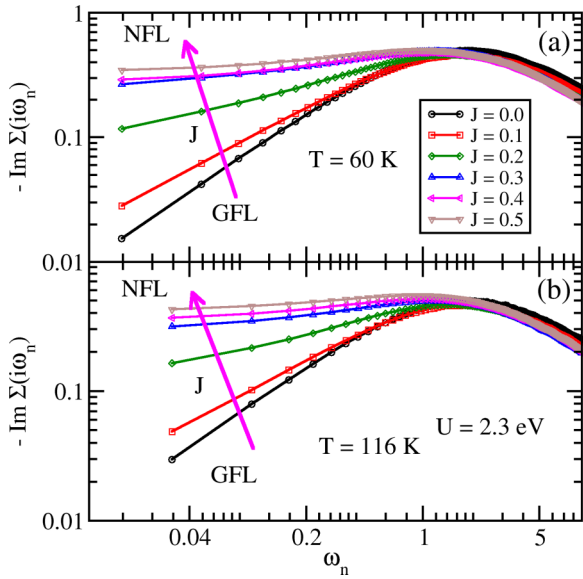


FIG. 5. Imaginary part of the Matsubara self-energy  $[-\text{Im}\Sigma(i\omega_n)]$  for  $U = 2.3$  eV and different  $J$  values for (a)  $T = 60$  K and (b)  $T = 116$  K.

Fermi liquid (GFL) form, i.e.,  $-\text{Im}\Sigma(i\omega_n) \sim a\omega_n^\alpha$ , where  $0 < \alpha \leq 1$ . As we increase  $J$ , a deviation from the power law is seen at low  $\omega_n$  as the  $-\text{Im}\Sigma(i\omega_n)$  acquires a nonzero intercept. The latter is characteristic of non-Fermi liquid behavior, where the imaginary part of the self-energy has a finite value as  $\omega_n \rightarrow 0$ . Thus as a function of increasing  $J$ , the single-particle dynamics exhibits a crossover from GFL to NFL that is driven by Hund's exchange [3]. The crossover is found to persist at a higher temperature  $T = 116$  K and is shown in Fig. 5(b).

A natural question arises about the choice of the  $U = 2.3$  eV for 3C-BaRuO<sub>3</sub>. Does this crossover from GFL to NFL survive with respect to variations in  $U$ ? The imaginary part of the self-energy for  $U = 3$  and 4 eV computed at a temperature  $T = 60$  K is shown in Fig. 6. Clearly, for  $U = 2.3$  and 3 eV, the intercept of the imaginary part of the self-energy is finite for  $J \gtrsim 0.2$  (from Fig. 5 and the top panel of Fig. 6), while for  $U = 4$  eV, a GFL form of  $-\text{Im}\Sigma(i\omega_n)$  is obtained for  $0 \leq J \leq 0.5$  eV. This implies that the NFL behavior for higher values of  $U$  ( $\gtrsim 4$  eV), if at all occurs, must be for  $J > 0.5$  eV. Hence, we conclude that the  $U_{\text{Ru}} = 2.3$  eV, corresponding to 3C-BaRuO<sub>3</sub> is somewhat special, since it places this material in a crossover region for *physically reasonable* values of the Hund's exchange.

Recent works on ruthenates found that the NFL behavior seen in the single-particle dynamics is characteristic of a finite temperature spin-frozen phase which crosses over to a Fermi liquid ground state at lower temperatures. This incoherent spin-frozen state [6] is characterized by finite intercepts in the imaginary part of the self-energy and fluctuating local moments (on the susceptibility). In order to better understand the crossover phase, we carry out a quantitative analysis of the imaginary part of the self-energy for many more  $J$  values in the same range as considered in Fig. 5. The imaginary part of the self-energy at low Matsubara frequencies is fit to the

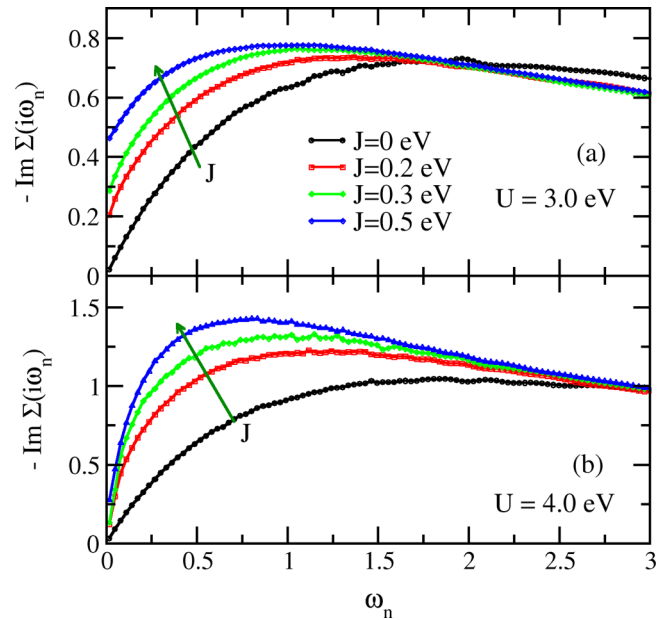


FIG. 6. Imaginary part of the self-energy for  $T = 60$  K and different  $J$  values (see legend) with (a)  $U = 3$  eV and (b)  $U = 4$  eV.

form [3]

$$-\text{Im}\Sigma(i\omega_n) \xrightarrow{\omega_n \rightarrow 0} C + A|\omega_n|^\alpha. \quad (1)$$

Figure 7 shows the exponent  $\alpha$  and intercept  $C$  as a function of  $J$  at various temperatures from 60 to 230 K, for  $U = 2.30$  eV. The exponent  $\alpha$  initially decreases with increasing  $J$ , goes through a minimum value of 0.5 at  $J \sim 0.25$  eV, and increases gradually for higher  $J$ . Werner *et al.* [3] found this behavior in a three orbital Hubbard model with fully rotationally invariant interactions for fixed filling ( $n = 2.0$ ) and Hund's exchange,

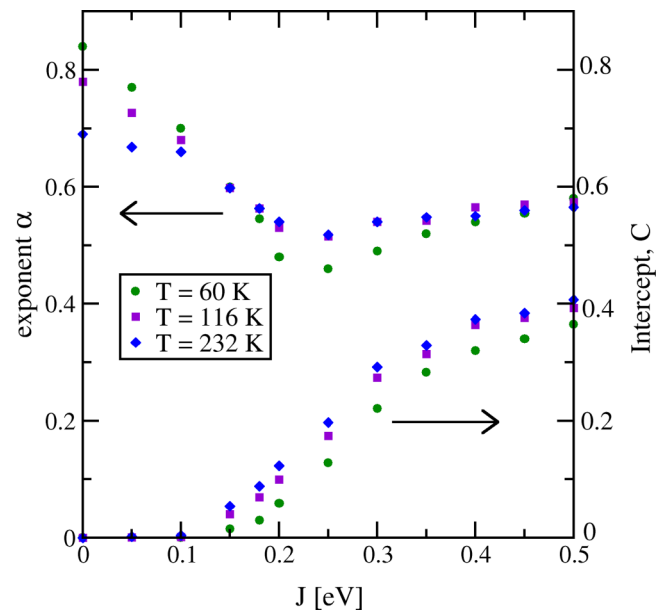


FIG. 7. Exponent  $\alpha$  (circles, left axis) and intercept  $C$  (squares, right axis) obtained by fitting the data to  $-\text{Im}\Sigma(i\omega_n) = C + A|\omega_n|^\alpha$  at different  $J$  values,  $U = 2.3$  eV and  $T = 60, 116,$  and  $232$  K.

but varying the  $U$  value. In our model the intercept  $C$  remains zero for  $J \lesssim 0.15$  eV and above that increases with  $J$ . Thus we identify a crossover Hund's exchange  $J_0 = 0.15$  eV such that for  $J < J_0$  the GFL phase exists, while for  $J > J_0$  the crossover NFL phase is found for  $\gtrsim 60$  K, where frozen moments are expected to scatter the conduction electrons. We have repeated the above analysis for  $U = 3$  eV and find that the crossover  $J_0 \sim 0.15$  eV is the same as that for  $U = 2.3$  eV within numerical tolerance.

It is interesting to note that the exponent  $\alpha$  in the GFL or in the NFL region is not equal to one. In the GFL phase, the exponent must approach one with decreasing temperature, and indeed, it does, as seen in Fig. 7 for  $J < J_0$ . Curiously, the exponent hardly changes with either temperature or  $J$  in the spin-frozen phase. Since a ferromagnetic transition occurs at  $T_c = 60$  K, it is likely that the spin-frozen phase is a precursor of the FM phase, and the local moments condense into a magnetically ordered state for  $T < 60$  K. Since even the intercept depends very weakly on temperature, the spin-frozen phase appears to be almost temperature independent. This implies that the NFL behavior should manifest in transport and thermal measurements over a wide range of temperatures from about 60 to at least 230 K.

The crossover function, given in Eq. (1), does not have a microscopic basis, and has been used purely as a fitting function. Since the latter is not unique, the identification of  $J_0$  must be verified through an alternative fit. Hence we have used a fourth order polynomial also to fit  $-\text{Im}\Sigma(i\omega_n)$  and confirm the robustness of  $J_0$ . The intercept  $C_0$  shown in the top panel of Fig. 8 does become finite only for  $J \gtrsim J_0$ . Thus, the identification of  $J_0$  remains robust. For a Fermi liquid, the linear coefficient of the self-energy  $C_1$  is related to the quasiparticle weight  $Z$  by  $C_1 = -(1 - 1/Z)$  at

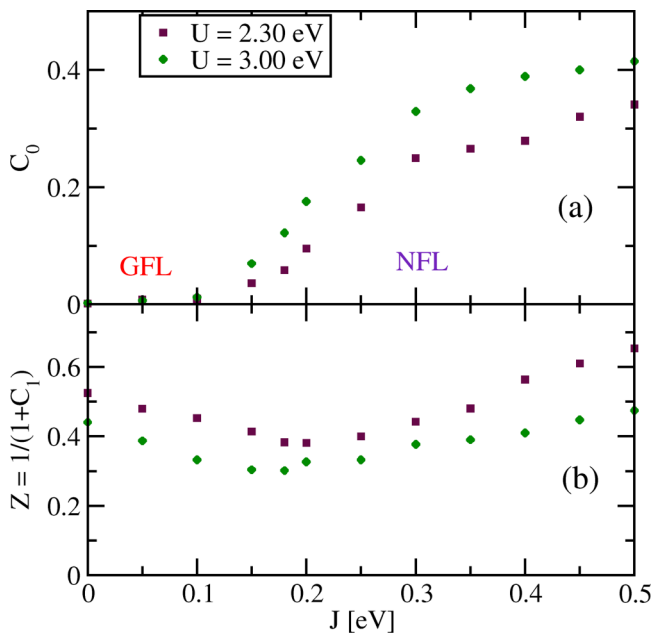


FIG. 8. Imaginary part of the self-energy  $[-\text{Im}\Sigma(i\omega_n)]$  fitted to a fourth order polynomial: (a) zeroth order coefficient  $C_0$ , (b)  $Z = 1/(1 + C_1)$ , where  $C_1$  is the linear coefficient, for different  $J$  values,  $U = 2.3$  and  $3.0$  eV and  $T = 60$  K.

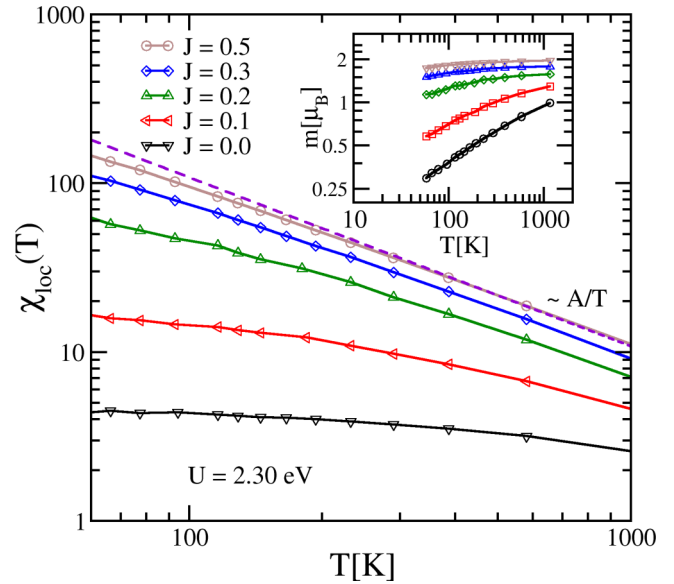


FIG. 9. Local static spin susceptibility as a function of temperature for different  $J$  values and  $U = 2.30$  eV. The dashed curve represents a  $1/T$  fit at high temperatures. Inset: The screened magnetic moment as a function of temperature.

$T = 0$ . Although  $C_1$  does not have the same interpretation at finite temperature, a qualitative picture may be obtained by examining the dependence of  $Z = 1/(1 + C_1)$ . The lower panel of Fig. 8 shows that  $Z$  decreases throughout the GFL phase. Although  $Z$  lacks any interpretation in the NFL phase ( $J > J_0$ ), a finite  $Z$  is, nevertheless, obtained which behaves in a similar way as the exponent of the power law fit (Fig. 7).

## B. Two-particle dynamics

The effect of temperature on spin correlations may be gauged through the local static spin susceptibility, given by  $\chi_{\text{loc}}(T) = \int_0^\beta d\tau \chi_{zz}(\tau)$ . Figure 9 shows  $\chi_{\text{loc}}(T)$  as a function of temperature for a range of  $J$  values. For  $J \lesssim 0.1$ ,  $\chi_{\text{loc}}(T)$  is very weakly dependent of temperature over the entire range shown, which is characteristic of Pauli-paramagnetic behavior and hence corresponds to a GFL. For larger  $J$  values, we observe local moment behavior [ $\chi_{\text{loc}}(T) \sim 1/T$ ] (see dashed line fit in the main panel). Thus with increasing  $J$ ,  $\chi_{\text{loc}}$  also crosses over to the local moment region from the GFL regime. We will see later that the temperature dependence of the susceptibility allows us to identify the value of the Hund's exchange coupling appropriate for 3C-BaRuO<sub>3</sub>. The inset shows the screened magnetic moment as a function of temperature computed through [25,26]  $m = \sqrt{T\chi(T)}$ . In the GFL phase ( $J < J_0$ ), the magnetic moment is seen to decrease monotonically with decreasing temperature indicating an absence of local moments at  $T = 0$ . While for  $J > J_0$ , the magnetic moment *appears* to saturate as  $T \rightarrow 0$  indicating fluctuating incoherent local moments in the spin-frozen phase.

In the 4d Ru-based TMOs, most theoretical studies are restricted to single-particle spectral functions and static susceptibilities [4,6]. There are only a few studies on two-particle spectral functions including vertex corrections [27], and even those are limited to fixed  $U$  and  $J$  values. In brief, there are

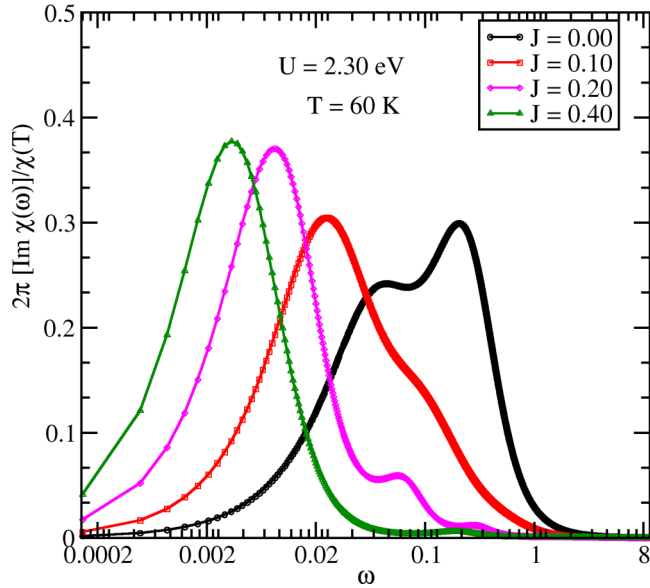


FIG. 10. Imaginary part of dynamical spin susceptibility on real frequency axis obtained from maximum entropy method for various  $J$  values,  $U = 2.3$  eV and  $T = 60$  K.

no studies available for the behavior of two-particle spectral functions (including vertex corrections) across the GFL to NFL crossover.

We have calculated the dynamical spin susceptibility  $\chi(\omega, T)$  on the real frequency axis by using the maximum entropy method [28,29]. In Fig. 10 we show the imaginary part of  $\chi(\omega, T)$  for various  $J$  values at  $U = 2.30$  eV and  $T = 60$  K. A large scale spectral weight transfer to the infrared occurs upon increasing  $J$ . Concomitantly, the half-width at half-maximum also decreases. The peak of  $\chi(\omega, T)$  represents the characteristic energy scale of the system [27,29], below which a Fermi liquid should emerge. The dramatic redshift of the peak with increasing  $J$  implies a strong suppression of the coherent scale [29–31]. Thus with increasing  $J$ , the energy scale for crossover from a low temperature Fermi liquid ground state to a high temperature incoherent phase decreases sharply. Since the only other scale (apart from the coherence scale) are the nonuniversal scales such as  $J$ , the bandwidth or  $U$ , the incoherent crossover phase should exist from very low temperatures to quite high temperatures. This explains the wide temperature range over which an incoherent spin-frozen phase, and the corresponding non-Fermi liquid behavior, is found, e.g., in the resistivity [1,8,11].

### C. Identification of $J$ for 3C-BaRuO<sub>3</sub>

Now we turn to an identification of model parameters appropriate for 3C-BaRuO<sub>3</sub> in the  $(U, J)$  plane. As mentioned earlier, we have chosen  $U_{\text{Ru}} = 2.3$  eV for 3C-BaRuO<sub>3</sub> which has been obtained through cRPA for its closely related cousins in the ruthenate family [6,7,32]. We obtain  $J_{\text{Ru}}$  by comparing the theoretically computed temperature dependent static susceptibility (from Fig. 9) with that of the experiment [8]. From experiments it is known that the saturated magnetic moment at 5 K (in the ferromagnetic state) is  $0.8 \mu_B/\text{Ru}$ , while the high temperature paramagnetic moment is  $2.6 \mu_B/\text{Ru}$ . Since

our theory is valid only in the nonmagnetic phase, we choose the latter for theoretical comparison. One more issue is the use of Ising-type or density-density type Hund's coupling usually underestimates the saturated magnetic moments, which results in a  $S = 1$  state corresponding to an ideal magnetic moment of  $2 \mu_B/\text{Ru}$  rather than  $2.8 \mu_B$  as would be expected for a true  $S = 1$  state with a rotationally invariant  $J$  term. Thus, the high temperature moment that we would be comparing to is  $(2.6/2.8) \times 2 = 1.86 \mu_B/\text{Ru}$ . We see from the inset of Fig. 9 that such a moment is obtained for  $J \sim 0.5$  eV. Hence we identify  $J_{\text{Ru}} \sim 0.5$  eV. We note that the experimentally measured  $\chi_{\text{loc}}^{-1}(T)$  is linear at high temperature, and deviates from linearity [8] at  $T \lesssim 150$  K. Again, such deviation from the high temperature  $1/T$  form in theoretical calculations is seen for  $J \sim 0.5$  at  $T \lesssim 150$  K (main panel of Fig. 9), thus lending support to the identification of  $J_{\text{Ru}} \sim 0.5$  eV. We have checked that the deviations from linearity occur at much higher temperatures ( $\gtrsim 300$  K) for  $J = 0.3$  and  $0.4$  eV, hence the error bar on  $J_{\text{Ru}}$  should be less than  $0.1$  eV. The value of Hund's coupling  $J_{\text{Ru}} \sim 0.5$  eV places 3C-BaRuO<sub>3</sub> deep in the incoherent spin-frozen phase for  $T \gtrsim 60$  K, and thus could explain the transition into a magnetically ordered state at  $T \lesssim 60$  K.

In addition to the static part, it would be interesting to see if the dynamics also contributes to the NFL behavior. Indeed the experimentally observed non-Fermi liquid behavior in  $\rho(T)$  could originate from an anomalous self-energy. Hence, we compute the real frequency self-energy through analytic continuation of the Matsubara  $\Sigma(i\omega_n)$  and display  $-\text{Im}\Sigma(\omega)$  (top panel) and the corresponding  $k$ -integrated spectrum,  $A(\omega) = -\text{Im}G(\omega)$  (bottom panel) for various temperatures in Fig. 11, where the local Green's function is

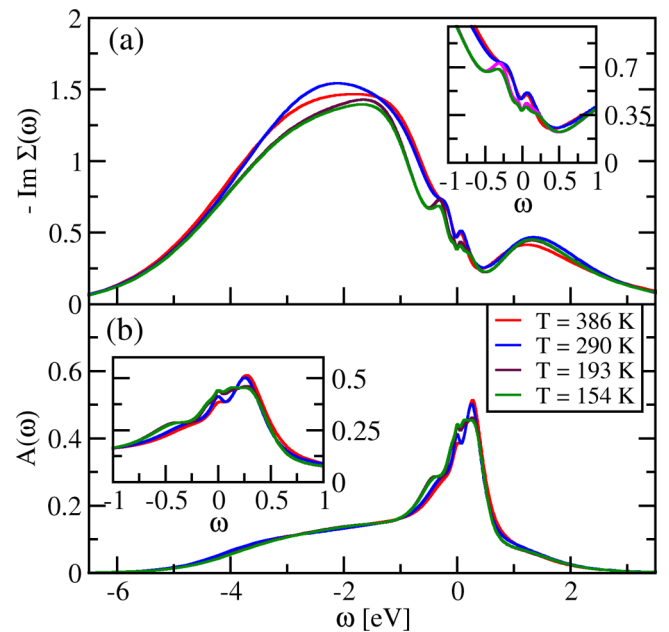


FIG. 11. (a) Imaginary part of the self-energy. (b) Single-particle spectral function on the real frequency axis obtained from the maximum entropy method for different temperatures and  $U = 2.3$  eV,  $J = 0.5$  eV.

given by

$$\begin{aligned} \mathbf{G}(\omega) &= \sum_k \mathbf{G}(k, \omega) \\ &= \sum_k \frac{1}{(\omega^+ + \mu)\mathbf{I} - \mathcal{H}_{\text{GGA}}(k) - \Sigma(\omega)}. \end{aligned} \quad (2)$$

Note that, within DMFT, the  $k$  dependence arises purely through the dispersion embedded in  $\mathcal{H}_{\text{GGA}}(k)$ . If the low-energy excitations are Fermi liquid like, then we should expect  $\text{Im}\Sigma(0) \propto -T^2$ . Figure 11(a) shows that the self-energy at the chemical potential has a finite and almost temperature-independent imaginary part. This feature, also displayed in Fig. 7, signifies that low-energy excitations are NFL in nature, and temperature does not have much effect on the value of  $\text{Im}\Sigma(0)$  in the spin-frozen phase. A very interesting insight into the dynamics of the spin-frozen phase comes from the low frequency form of the self-energy. The inset zooms in onto the low frequency part of  $-\text{Im}\Sigma(\omega)$ , which is seen to have a form  $\sim C + A\omega^2$  that is usually found in disordered Fermi liquids [33]. Such a form is consistent with the scenario of incoherent and fluctuating local moments in the spin-frozen phase.

The single-particle spectral function  $A(\omega)$  shown in Fig. 11(b) has an overall line shape very similar to that of SrRuO<sub>3</sub> [34] and Sr<sub>2</sub>RuO<sub>4</sub> [1]. A metallic nature is indicated by a finite weight at the Fermi level. A closer look at the temperature dependence at low frequencies shows the emergence of structures that presumably correspond to transitions between the various multiplets of the atomic limit. However, a far more detailed study, varying  $U$  and  $J$ , is required for a precise identification of the origin of these features. Since analytic continuation using the maximum entropy method requires immense computational resources, especially in the spin-frozen phase, we have not attempted to carry out such a study in the present work.

Experiments can probe single-particle dynamics in the spin-frozen phase through, e.g., angle-resolved photoemission spectroscopy (ARPES). Theoretically we can predict the ARPES line shape through a calculation of the momentum-resolved spectral function given by  $A(k, \omega) = -\text{Im}G(k, \omega)/\pi$ . In Fig. 12 we plot the intensity map of the momentum-resolved spectral function  $A(k, \omega)$  of 3C-BaRuO<sub>3</sub> obtained from DFT by simply ignoring the self-energy in Eq. (2) (top panel) and then compared with the results of DFT+DMFT (lower panel) at  $T = 154$  K for  $U_{\text{Ru}} = 2.3$  eV and  $J_{\text{Ru}} = 0.5$  eV. In the case of DFT, the quasiparticle bands have a minimum at the  $\Gamma$  point ( $-2.3$  eV) and a maximum at  $R$  point ( $0.8$  eV). When we turn on interactions (DFT+DMFT), the first striking feature that emerges is that there are no quasiparticle bands. But, even though each of the bands acquires a finite width when interactions are introduced, there is a resemblance between the quasiparticle bands in the spectral function map and the DFT spectra. The “fat bands” are simply a result of the finite scattering rate arising from the imaginary part of the self-energy (Fig. 11). Furthermore, although the bands in DFT as well as DFT+DMFT have a minimum and maximum exactly at the same high symmetry points, the values of corresponding energies renormalize to  $-4.8$  and  $1.0$  eV, respectively. The

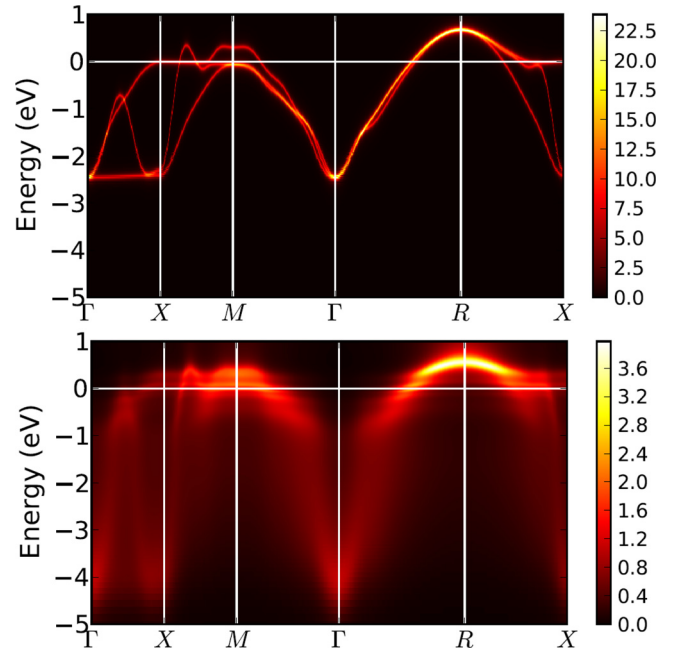


FIG. 12. Intensity map of the spectral function  $A(k, \omega)$  obtained from DFT (top panel) and DFT+DMFT (lower panel) for  $U = 2.3$  eV,  $J = 0.5$  eV at  $T = 154$  K plotted along high symmetry directions in the irreducible Brillouin zone.

bands below  $-1.0$  eV (incoherent regime) are much more broadened [6,34] in comparison with the those closer to the Fermi level, which again is a manifestation of the peak in the imaginary part of the self-energy around  $-2$  eV.

For the values of  $U_{\text{Ru}} = 2.3$  eV and  $J_{\text{Ru}} \sim 0.5$  eV, we obtain a relatively modest effective mass  $\frac{m^*}{m_{\text{GGA}}}$  of 1.56 at  $T = 60$  K. A definitive comment about the effective mass in the ground state cannot be made with the preceding estimate at finite temperature, since the quasiparticle weight has a proper meaning [35] only below the Fermi liquid coherence scale, which is strongly suppressed for  $J = 0.5$  (as compared to  $J = 0$ ) as seen from the dynamical susceptibility results (from Fig. 10). The strong suppression of the Fermi liquid scale suggests that 3C-BaRuO<sub>3</sub> could be very strongly correlated. Here we would like to comment on the value of  $U$  ( $= 4.0$  eV) and  $J$  ( $= 0.6$  eV) chosen in a previous work [36], where the interaction parameters were obtained from a “local spin density approximation constraint” technique. For those parameters, a recent study of one of the  $4d$  Ruthenium compounds [7] within a five  $d$ -band model finds that correlations are induced due to the proximity to a Mott insulating state, which concurs with our results for a three  $d$ -band model (from the lower panel of Fig. 2). However, the proximity of a Mott insulating state does not violate adiabatic continuity and hence as shown above, the choice of  $(U, J) = (4.0, 0.6)$  eV would not explain several anomalous features of 3C-BaRuO<sub>3</sub> including the wide  $1/T$  behavior of  $\chi_{\text{loc}}(T)$ , or the NFL behavior of resistivity. These and the transition to a ferromagnetically ordered state at low temperature are naturally explained by the presence of a spin-frozen phase as found for  $U_{\text{Ru}} = 2.3$  eV and  $J_{\text{Ru}} \sim 0.5$  eV.

#### IV. CONCLUSIONS

We have studied 3C-BaRuO<sub>3</sub> in the nonmagnetic phase by using GGA+DMFT (HY-CTQMC). In the dynamical correlation functions and static spin susceptibility, we observed a crossover from GFL to NFL driven by the Hund's exchange  $J$ . A fitting of the self-energy to a power law function determines the crossover boundary, i.e.,  $J_0 = 0.15$  eV. The local, on-site Coulomb repulsion  $U_{\text{Ru}} = 2.3$  eV was chosen to be the same as that found through a constrained random phase approximation calculations for the closely related SrRuO<sub>3</sub>. We determine the Hund's exchange  $J_{\text{Ru}} \sim 0.5$  eV, appropriate for 3C-BaRuO<sub>3</sub> such that the computed high temperature paramagnetic moment matches the experimentally found value. Nonmagnetic calculations with these parameters ( $U_{\text{Ru}}$ ,  $J_{\text{Ru}}$ ) for single-particle dynamics and static spin susceptibility show that cubic-BaRuO<sub>3</sub> is in a spin-frozen state at temperatures above the ferromagnetic transition point. Future calculations

incorporating symmetry broken states should reveal the causal relation between the high temperature spin-frozen phase and the dynamics in the low temperature ferromagnetic phase.

#### ACKNOWLEDGMENTS

We thank CSIR and DST (India) for research funding. This work is partly supported by NSF DMR-1237565 (N.S.V. and J.M.) and NSF EPSCoR Cooperative Agreement EPS-1003897 with additional support from the Louisiana Board of Regents (N.D. and M.J.). N.D. thanks Swapan K. Pati for helpful discussions. Our simulations used an open source implementation [37] of the hybridization expansion continuous-time quantum Monte Carlo algorithm [17] and the ALPS [38] libraries. The computational resources are provided by the Louisiana Optical Network Initiative (LONI) and HPC@LSU.

- 
- [1] A. Georges, L. de'Medici, and J. Mravlje, *Annu. Rev. Condens. Matter Phys.* **4**, 137 (2013).
- [2] J. Zhao, L. Yang, Y. Yu, F. Li, R. Yu, Z. Fang, L. Chen, and C. Jin, *J. Solid State Chem.* **180**, 2816 (2007).
- [3] P. Werner, E. Gull, M. Troyer, and A. J. Millis, *Phys. Rev. Lett.* **101**, 166405 (2008).
- [4] K. Haule and G. Kotliar, *New J. Phys.* **11**, 025021 (2009).
- [5] L. de'Medici, J. Mravlje, and A. Georges, *Phys. Rev. Lett.* **107**, 256401 (2011).
- [6] J. Mravlje, M. Aichhorn, T. Miyake, K. Haule, G. Kotliar, and A. Georges, *Phys. Rev. Lett.* **106**, 096401 (2011).
- [7] H. T. Dang, J. Mravlje, A. Georges, and A. J. Millis, *Phys. Rev. B* **91**, 195149 (2015).
- [8] C.-Q. Jin, J.-S. Zhou, J. B. Goodenough, Q. Q. Liu, J. G. Zhao, L. X. Yang, Y. Yu, R. C. Yu, T. Katsura, A. Shatskiy, and E. Ito, *Proc. Natl. Acad. Sci. USA* **105**, 7115 (2008).
- [9] G. Cao, S. McCall, M. Shepard, J. E. Crow, and R. P. Guertin, *Phys. Rev. B* **56**, 321 (1997).
- [10] J.-S. Zhou, K. Matsubayashi, Y. Uwatoko, C.-Q. Jin, J.-G. Cheng, J. B. Goodenough, Q. Q. Liu, T. Katsura, A. Shatskiy, and E. Ito, *Phys. Rev. Lett.* **101**, 077206 (2008).
- [11] P. B. Allen, H. Berger, O. Chauvet, L. Forro, T. Jarlborg, A. Junod, B. Revaz, and G. Santi, *Phys. Rev. B* **53**, 4393 (1996).
- [12] Y. S. Lee, J. Yu, J. S. Lee, T. W. Noh, T.-H. Gimm, H.-Y. Choi, and C. B. Eom, *Phys. Rev. B* **66**, 041104 (2002).
- [13] G. Kotliar, S. Y. Savrasov, K. Haule, V. S. Oudovenko, O. Parcollet, and C. A. Marianetti, *Rev. Mod. Phys.* **78**, 865 (2006).
- [14] J. P. Perdew, K. Burke, and M. Ernzerhof, *Phys. Rev. Lett.* **77**, 3865 (1996).
- [15] A. Georges, G. Kotliar, W. Krauth, and M. J. Rozenberg, *Rev. Mod. Phys.* **68**, 13 (1996).
- [16] E. Gull, A. J. Millis, A. I. Lichtenstein, A. N. Rubtsov, M. Troyer, and P. Werner, *Rev. Mod. Phys.* **83**, 349 (2011).
- [17] P. Werner, A. Comanac, L. de'Medici, M. Troyer, and A. J. Millis, *Phys. Rev. Lett.* **97**, 076405 (2006).
- [18] P. Giannozzi, S. Baroni, N. Bonini, M. Calandra, R. Car, C. Cavazzoni, D. Ceresoli, G. L. Chiarotti, M. Cococcioni, I. Dabo, A. Dal Corso, S. de Gironcoli, S. Fabris, G. Fratesi, R. Gebauer, U. Gerstmann, C. Gougoussis, A. Kokalj, M. Lazzeri, L. Martin-Samos, N. Marzari, F. Mauri, R. Mazzarello, S. Paolini, A. Pasquarello, L. Paulatto, C. Sbraccia, S. Scandolo, G. Sclauzero, A. P. Seitsonen, A. Smogunov, P. Umari, and R. M. Wentzcovitch, *J. Phys. Condens. Matter* **21**, 395502 (2009).
- [19] J. P. Perdew, K. Burke, and Y. Wang, *Phys. Rev. B* **54**, 16533 (1996).
- [20] N. Marzari and D. Vanderbilt, *Phys. Rev. B* **56**, 12847 (1997).
- [21] A. A. Mostofi, J. R. Yates, Y.-S. Lee, I. Souza, D. Vanderbilt, and N. Marzari, *Comput. Phys. Commun.* **178**, 685 (2008).
- [22] A. E. Antipov, I. S. Krivenko, V. I. Anisimov, A. I. Lichtenstein, and A. N. Rubtsov, *Phys. Rev. B* **86**, 155107 (2012).
- [23] H. Ishida and A. Liebsch, *Phys. Rev. B* **81**, 054513 (2010).
- [24] S. Biermann, L. de'Medici, and A. Georges, *Phys. Rev. Lett.* **95**, 206401 (2005).
- [25] H. R. Krishnamurthy, J. W. Wilkins, and K. G. Wilson, *Phys. Rev. B* **21**, 1003 (1980).
- [26] P. Hansmann, R. Arita, A. Toschi, S. Sakai, G. Sangiovanni, and K. Held, *Phys. Rev. Lett.* **104**, 197002 (2010).
- [27] A. Toschi, R. Arita, P. Hansmann, G. Sangiovanni, and K. Held, *Phys. Rev. B* **86**, 064411 (2012).
- [28] M. Jarrell and J. E. Gubernatis, *Phys. Rep.* **269**, 133 (1996).
- [29] M. Jarrell, J. E. Gubernatis, and R. N. Silver, *Phys. Rev. B* **44**, 5347 (1991).
- [30] C. Raas and G. S. Uhrig, *Phys. Rev. B* **79**, 115136 (2009).
- [31] N. Dasari, S. Acharya, A. Taraphder, J. Moreno, M. Jarrell, and N. Vidhyadhiraja, *arXiv:1509.09163*.
- [32] Z. V. Pchelkina, I. A. Nekrasov, T. Pruschke, A. Sekiyama, S. Suga, V. I. Anisimov, and D. Vollhardt, *Phys. Rev. B* **75**, 035122 (2007).
- [33] N. S. Vidhyadhiraja and P. Kumar, *Phys. Rev. B* **88**, 195120 (2013).

- [34] M. Kim and B. I. Min, [Phys. Rev. B](#) **91**, 205116 (2015).
- [35] L. Fanfarillo and E. Bascones, [Phys. Rev. B](#) **92**, 075136 (2015).
- [36] L. Huang and B. Ao, [Phys. Rev. B](#) **87**, 165139 (2013).
- [37] H. H. Hafermann, P. Werner, and E. Gull, [Comput. Phys. Commun.](#) **184**, 1280 (2013).
- [38] B. Bauer *et al.*, [J. Stat. Mech.](#) (2011) P05001.